Available online at www.sciencedirect.com
ScienceDirect
Trans. Nonferrous Met. Soc. China 35(2025) 3256−3271
Transactions of Nonferrous Metals Society of China
www.tnmsc.cn

Preparation of high-strength and high-ductility Mg−Gd−Y−Zn−Zr alloy via deformation at low temperature and small extrusion ratio

Ya-yun HE[1], Rui GUO[2], Xi ZHAO[1,2], Zhi-min ZHANG[3]

1. College of Mechanical and Electrical Engineering, North University of China, Taiyuan 030051, China;
2. School of Aeronautics and Astronautics, North University of China, Taiyuan 030051, China;
3. College of Materials Science and Engineering, North University of China, Taiyuan 030051, China

Received 17 May 2024; accepted 24 February 2025

Abstract: A method of pre-regulating the lamellar long-period stacking ordered (LPSO) phase was introduced to enhance the hot plasticity of rare earth magnesium alloys. Additionally, low-temperature extrusion was used to achieve a comprehensive improvement of alloy performance with small deformation, providing a new approach for the preparation of high-performance large components. The strengthening−toughening mechanism under low-temperature extrusion with an extrusion ratio of 3.6:1 was investigated by comparing the microstructure and performance of pre-regulated Mg−Gd−Y−Zn−Zr alloy at three different extrusion temperatures (420, 450, and 480 °C). Results show that the alloy extruded at 420 °C exhibits a yield strength of 341 MPa, tensile strength of 419 MPa, and elongation of 7.2%. The increase in strength is mainly caused by the strong texture and internal dislocation pinning of the undynamic recrystallization (un-DRX) zone, and a lower volume fraction of β dynamic precipitation phase is beneficial to improving the ductility of the alloy.
Key words: 14H-LPSO lamellar phase; Mg−Gd−Y−Zn−Zr alloy; low-temperature extrusion; β dynamic precipitation phase

1 Introduction

The Mg−RE (rare earth)−Zn-based alloys reinforced with long-period stacking ordered (LPSO) structures exhibit higher strength, better ductility, and better heat resistance compared to conventional magnesium alloys, making them widely used in aerospace, defense and military industries [1]. Research on the LPSO phase shows that this kind of heterostructure can effectively improve the strength of the material. YOSHIHITO et al [2] prepared an ultra-high strength magnesium alloy by rapid solidification powder metallurgy, which has a yield strength of 610 MPa and an elongation of 5% at room temperature. The ultra-high strength is attributed to the precipitation of the LPSO phase within the crystal structure. XU et al [3] prepared a high-strength and high-ductility alloy containing the LPSO phase through hot extrusion technology. This alloy exhibited a tensile yield strength (TYS) of 356 MPa, ultimate tensile strength (UTS) of 419 MPa, and elongation at break (FE) of 17.2%. The excellent properties of the LPSO phase provide better plastic deformation ability. For example, HAGIHARA et al [4] investigated the plastic deformation mechanism of the 14H-typed LPSO phase under compression. It was found that a deformation kink zone is formed under compression when the basal slip is suppressed. WU et al [5] studied the deformation mechanism of the LPSO phase in equal channel extrusion of $Mg_{94}Zn_2Y_4$ alloy. They found that the kink of the LPSO phase can promote dynamic

Corresponding author: Xi ZHAO, Tel: +86-13934204597, E-mail: zhaoxi_1111@163.com
https://doi.org/10.1016/S1003-6326(25)66879-8

recrystallization to a certain extent. In summary, a large number of studies have shown that the lamellar LPSO phase can effectively improve plasticity at room temperature. Pre-regulating the lamellar phase morphology can promote non-basal slip and induce continuous recrystallization, triggering a series of reactions that improve the deformation coordination ability. More importantly, it is possible to form a stress balance mechanism, inhibit crack initiation, and enhance the hot-forming ability of the alloy.

The strengthening−toughening mechanism of magnesium alloys has long been a hot issue. Adding rare earth elements is an effective way to improve the strength [6,7]. Studies have shown that rare earth elements, such as Gd and Y, can produce significant solid solution strengthening and aging-strengthening effects [8]. The precipitation of β' phase during the aging process of Mg−Gd−Y alloy can effectively improve the strength of the alloy [9]. In addition, scholars have also achieved very good strengthening−toughening effects by adding Mn, Zr elements [10] and Sn elements [11]. However, the unstable supply and high cost of rare earth elements limit their widespread application. In addition, regulating the precipitation of the precipitated phase by heat treatment can improve the strength, but to a certain extent, it sacrifices the ductility [8]. In contrast, plastic forming can improve the strength and plasticity of the alloy at the same time, which is considered to be the best way to improve the performance of magnesium alloy. The existing high-performance magnesium alloys are reported to be obtained by ultra-high extrusion ratio and large deformation. For example, the extrusion ratio can reach 10:1 [12], 16:1 [13], and 20:1 [14]. The reason is that ultra-high deformation can obtain finer grain structure, leading to enhanced strength and ductility. However, due to equipment limitations, the preparation of large components can only be achieved through a small deformation degree (generally the extrusion ratio is less than 5). Since it is difficult to replicate the deformation process of small specimens, the performance of these large components often falls short of that observed in small specimens. Consequently, improving the performance of components at lower extrusion ratios has become a significant global challenge.

It is worth noting that some scholars have achieved the synergistic improvement of strength and ductility of magnesium alloys through low-temperature deformation. For example, ZHAI et al [15] reported that low-temperature extrusion of Mg−Bi−Ca alloy resulted in a tensile yield strength of ~397.1 MPa, an ultimate tensile strength of ~416.2 MPa, and an acceptable elongation of ~8%. YU et al [12] investigated the effect of temperature on the microstructure and mechanical properties of as-extruded Mg−11.5Gd−4.5Y−(1Nd/1.5Zn)−0.3Zr (wt.%) alloy. The mechanical properties of the alloy included a tensile yield strength (TYS) of 371 MPa, an ultimate tensile strength (UTS) of 424 MPa, and a fracture elongation (FE) of 7.2%. In summary, low-temperature extrusion can usually obtain a favorable microstructure, with strengthening achieved by controlling the grain size, texture, and the number of precipitates, thereby enhancing the mechanical properties of the alloy [16−19]. These studies suggest that conducting plastic forming of components under low-temperature conditions could significantly improve their mechanical properties. In recent years, a growing number of researchers have focused on using strong basal textures to enhance mechanical properties [20,21]. A strong basal texture can be obtained not only through low temperature and rapid extrusion but also via small deformation. For instance, LI et al [22] prepared a binary Mg−13Gd (wt.%) wrought alloy by traditional extrusion process with an extrusion ratio of 4. The results demonstrated that a high strength of above 500 MPa under tension can be readily achieved in the 85% un-DRX alloy by effectively utilizing both texture strengthening and precipitation strengthening. Overall, these studies have partially validated the feasibility of low-temperature extrusion strengthening technology.

Magnesium has a typical hexagonal close-packed crystal structure, which limits its ability to undergo plastic deformation, making low-temperature extrusion particularly challenging. However, previous studies have shown promising results, indicating that the high temperature plasticity of rare earth magnesium alloy can be improved by pre-regulating the precipitation of lamellar 14H-LPSO. In this study, the plastic deformation behavior and mechanical properties of Mg−Gd−Y−Zn−Zr alloys with pre-regulated LPSO phases at different temperatures and under small deformation are investigated. The aim is to gain a deeper understanding of the plastic deformation mechanism, as well as the strengthening−toughening mechanism of alloys under low extrusion ratios and low temperatures. This research will contribute to more comprehensive understanding of plastic deformation mechanism of rare earth magnesium alloys and provide new insights for the strengthening of large components made from these materials.

2 Experimental

The material used in this experiment was Mg−13Gd−4Y−2Zn−0.5Zr magnesium alloy rod, formed by upsetting and extrusion after semi-continuous casting, with a size of *d*330 mm × 1000 mm. Its compositions are shown in Table 1.

Table 1 Compositions of Mg−13Gd−4Y−2Zn−0.5Zr (wt.%)

Mg	Gd	Y	Zn	Zr	Si	Cu	Fe
Bal.	12.88	4.00	2.00	0.50	<0.01	<0.01	<0.01

The alloy obtained by three times of upsetting and extrusion was heat treated at (510 °C, 18 h) + (480 °C, 1 h). To investigate the effect of thermal deformation at different temperatures on the microstructure and mechanical properties, a forward extrusion experiment was conducted on the heat-treated samples with an extrusion ratio of 3.6:1. Three extrusion temperatures were selected in the study: 420, 450, and 480 °C. The forward extrusion die diagram is shown in Fig. 1.

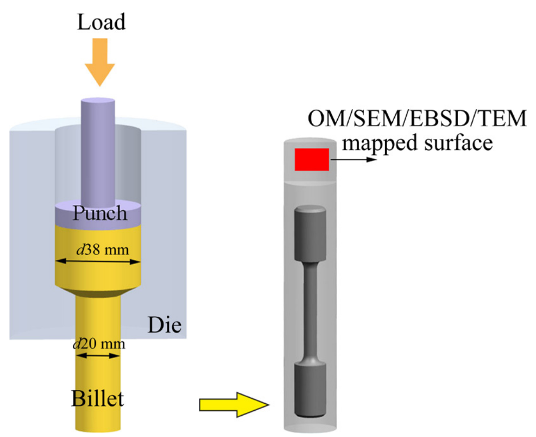

Fig. 1 Forward extrusion experiment and sampling diagram

The samples were polished on 600#, 1000#, 2000#, 3000#, 5000#, 7000# sandpapers in turn. The finely ground samples were then polished to a scratch-free, mirror-like finish by an MP-2A endless variable speed grinding and polishing machine with flannel. The corrosion solution was prepared, consisting of 1 g of picric acid, 2 mL of deionized water, 2 mL of glacial acetic acid, and 14 mL of anhydrous ethanol. The polished samples were etched in the solution for 5 s and then rinsed with alcohol. The metallographic observation was conducted using a ZEIS-Image optical metallographic microscope.

In this experiment, SEM and BSE experiments were carried out using a Hitachi SU−5000 scanning electron microscope to characterize the evolution of microstructure at high magnification. The surface morphology and phase changes of the deformed samples were observed and analyzed to further elucidate the relationship among phase morphology, grain evolution, and deformation mechanism. The area fractions of the β phase were quantified from SEM images using IPP6.0 software. To ensure statistical accuracy, at least three images were analyzed for each sample.

Additionally, polished samples were subjected to ion thinning on a Leica ion thinning instrument at a voltage of 6.5 kV. After thinning for 35 min, the samples were used for EBSD detection in Hitachi SU−5000 scanning electron microscope. The scanned area included grains larger than 200 μm, with a scanning step size ranging from 0.8 to 1.2 μm. After experiment, the data were processed by OIM (orientation imaging microscopy) Analysis-v7.0 software. To accurately count the DRX volume fraction, recrystallised grains were singled out in the OIM software according to the grain orientation spread (GOS) criterion (<2° for recrystallised grains), and the area fractions of the DRX were measured using IPP6.0 software.

For the preparation of TEM samples, thin sheets with a thickness of 80−100 μm, smooth surface, and no scratches were prepared by wire cutting and mechanical grinding. Round sheets with a diameter of 3 mm were then punched out using a punching machine. The thin areas required for transmission electron microscopy observation were prepared by a twin-jet electropolisher. The composition of the twin-jet liquid was 15 mL perchloric acid and 285 mL ethanol. The working current for the electropolisher was maintained at about 10 mA, and the temperature of the liquid was about −40 °C. After the sample was perforated, it was gently placed in ethanol for cleaning. After cleaning, the samples were dried with filter paper to remove surface moisture and immediately observed under a microscope. Bright-field image (BF) and selected area electron diffraction (SAED) were performed on the samples using an FEI Tecnai G20 field emission transmission electron microscope and a Titan G2 60−300 objective lens spherical aberration correction field emission transmission electron microscope. High-angle annular dark field (HAADF) imaging was performed by Titan to observe the atomic stacking and atomic segregation of the second phase.

In this study, the mechanical properties of samples were tested. To obtain accurate results, rod-shaped sample was used in the tensile test, as shown in Fig. 1. The tensile test was carried out using an Instron 3382 electronic tensile testing machine at a tensile rate of 1 mm/min. The yield strength and tensile strength of different samples were obtained by extensometer, and three samples were tested under the same conditions to ensure consistency.

3 Results

3.1 Microstructure before hot extrusion

Figure 2 shows the initial microstructure of the alloy. There is a small amount of bulk LPSO phase

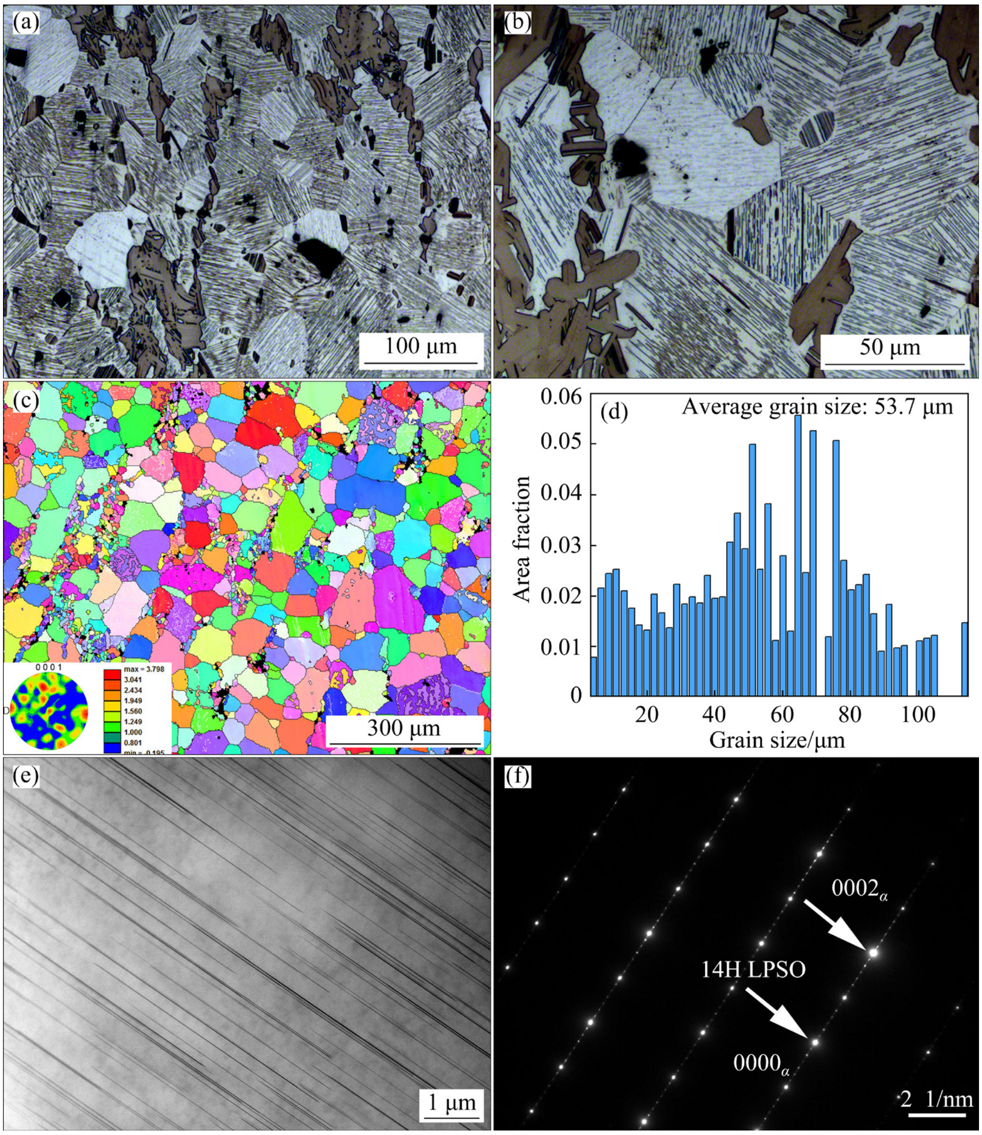

Fig. 2 Initial microstructure of alloy: (a, b) Optical microstructure; (c) Inverse pole figure map; (d) Grain size distribution; (e) TEM image; (f) SAED pattern of 14H-LPSO phase

in the intercrystalline region, and the lamellar 14H-LPSO phase with a narrow spacing is densely distributed in the crystal. Figure 2(c) shows the LPSO phase captured under TEM bright-field conditions with incident light beam of $\boldsymbol{B}$=[$11\bar{2}0$]. The LSPO phase is observed to be dense, with an interlamellar spacing of about 0.5 μm. The corresponding diffraction spot of the LPSO phase is shown in Fig. 2(f). The IPF diagram of the initial microstructure is given in Fig. 2(d), which indicates a weak 0001 texture and random grain orientation. The average grain size calculated by EBSD is 53.7 μm.

3.2 Microstructure after hot extrusion

Figure 3 shows the optical microstructures (OM) of alloy extruded at different temperatures. Figures 3(a−c) show the microstructure at low magnification, and Figs. 3(d−f) show the enlarged microstructure. Upon examining the metallographic images, it can be observed that the equiaxed large grains are elongated along the extrusion direction and distributed along the extrusion streamline. The narrow lamellar 14H-LPSO phase within the grains is severely kinked after extrusion deformation, and the lamellar LPSO phase aligns parallel to the extrusion direction after extrusion. This is related to the crystallographic orientation of the lamellar LPSO phase [23] and the formation of the extrusion texture of magnesium alloy. At an extrusion temperature of 420 °C, dynamically recrystallized (DRX) grains are arranged in a necklace-like pattern around the un-DRX zone, as indicated by the red arrows in Fig. 3(d). When the extrusion temperature increases to 450 °C, the location of the DRX changes; it not only appears around the un-DRX zone but also begins to form within the parent grains, as shown by the yellow arrows in Fig. 3(e). Moreover, when extrusion temperature reaches 480 °C, the DRX size increases, and the large grains are gradually divided, as indicated by the blue arrows in Fig. 3(f).

Figure 4 shows the IPF diagrams of the transverse and longitudinal sections of extruded alloy at different temperatures and the texture pole figures of the corresponding (0001) and ($10\bar{1}0$) planes. In the figure, the high-angle grain boundaries (15°−180°) are indicated by black lines, and the low-angle grain boundaries (2°−15°) are marked with white lines. The EBSD cross-sectional analysis reveals that the proportion of the DRX gradually increases with the extrusion temperature. Specifically, the calculated DRX volume fractions for the alloy extruded at 420, 450, and 480 °C are 28%, 31%, and 58%, respectively. Additionally, the size of the DRX grains also increases with extrusion temperature, measuring 3.41, 3.52, and 5.86 μm, respectively. Overall, the average grain sizes for samples extruded at 420, 450, and 480 °C are 24, 22 and 20 μm, respectively.

Further analysis of the texture of the extruded rod is shown in the extrusion texture pole figures

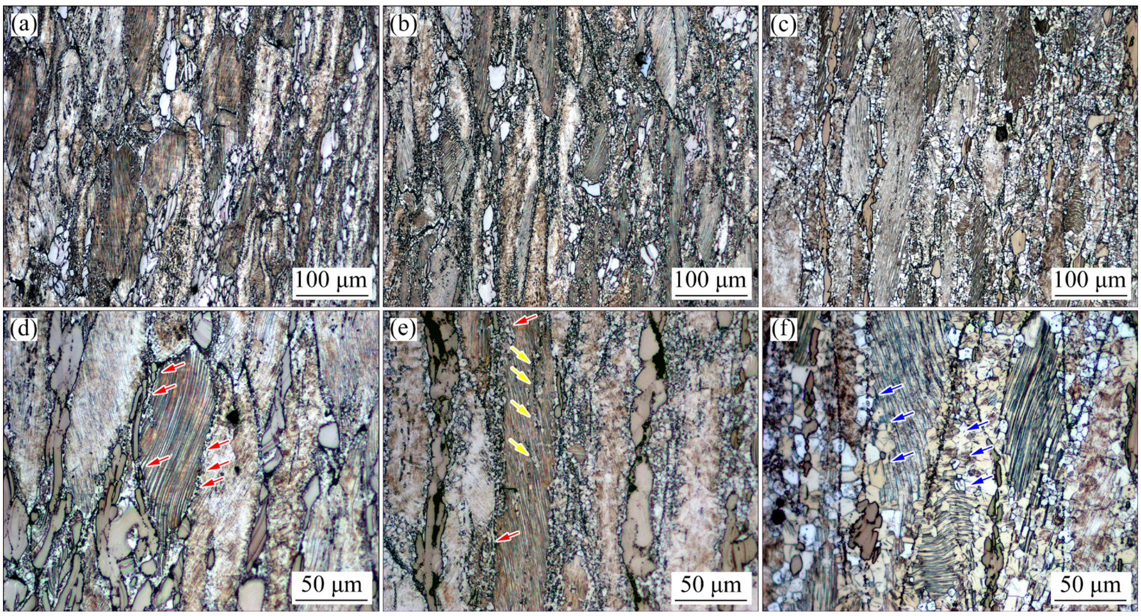

Fig. 3 Optical microstructures of extruded alloys at different temperatures: (a, d) 420 °C; (b, e) 450 °C; (c, f) 480 °C

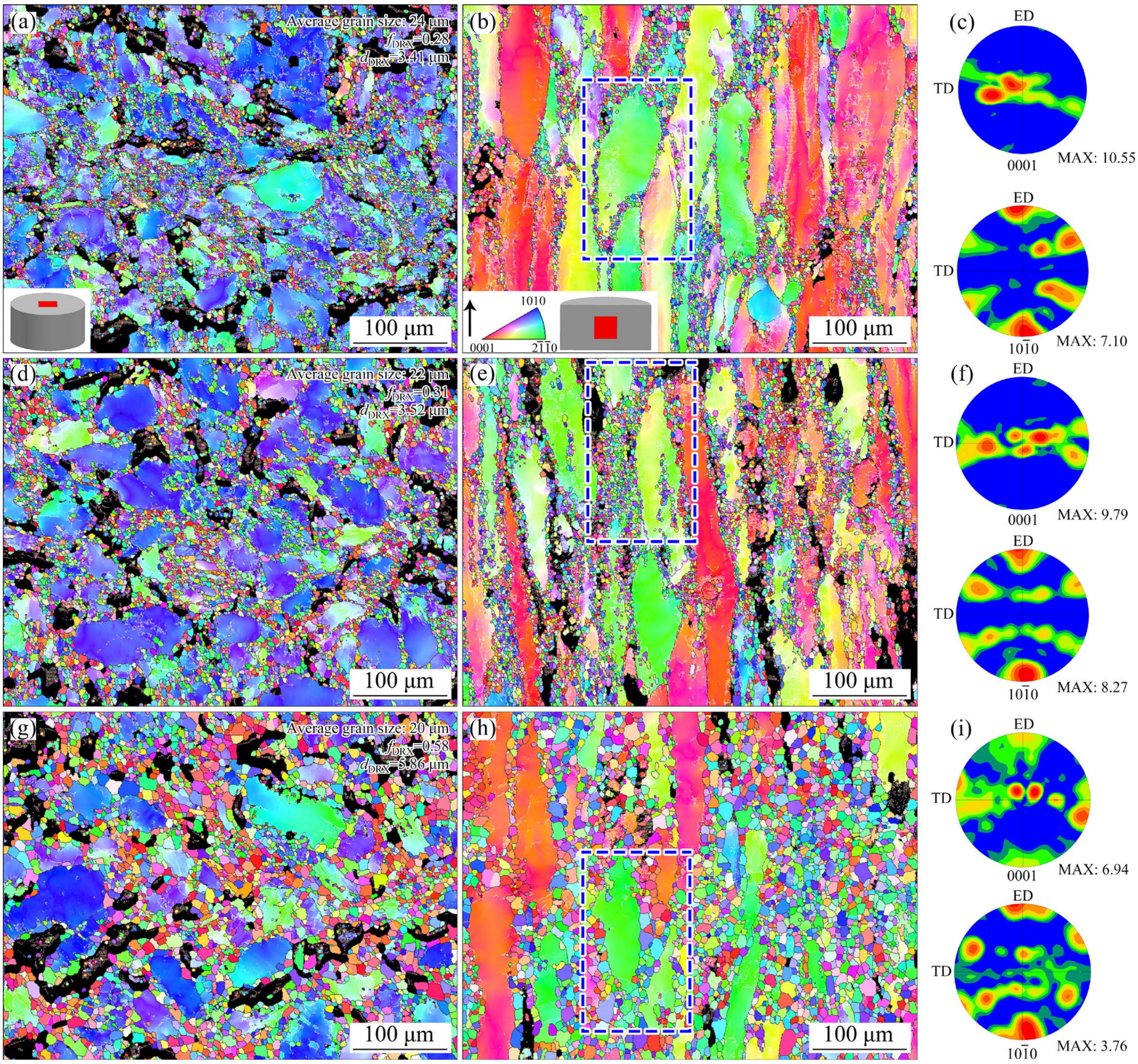

Fig. 4 IPF diagrams and texture diagrams of alloys at different extrusion temperatures: (a−c) 420 °C; (d−f) 450 °C; (g−i) 480 °C; (a, d, g) Cross section; (b, e, f) Longitudinal section

(Figs. 4(c, f, i)). The (0002) basal plane is parallel to the extrusion direction. However, with the increase in temperature, the texture intensity decreases from 10.55 at 420 °C to 9.79 at 450 °C, and finally to 6.94 at 480 °C. This decrease in basal texture intensity correlates with the increasing volume fraction of DRX.

In addition, the distribution of the local misorientation (KAM map) is shown in Figs. 5(a−c). The color scale indicates that local dislocation density gradually increases as the color shifts from blue to red. It can be seen from the KAM map that as the deformation temperature increases, the main color of the image changes from green to blue. As the extrusion temperature increases, the average KAM value of the sample gradually decreases from 0.97 to 0.91, and eventually to 0.61. From the color strips, the higher dislocation density is mainly in the coarse grain region, while the dislocation density in the fine grain region is lower. With the increase of extrusion temperature, the average dislocation density decreases, which aligns with the increasing DRX fraction. These results suggest that a greater number of dislocations accumulate in the coarse grains due to the lower DRX fraction of low-temperature deformation.

Figure 6 presents the SEM images of the longitudinal section of the extruded alloy rod at different temperatures, revealing three types of second phases formed after extrusion. The first is the block-shaped LPSO phase at grain boundary, which exists throughout the entire deformation

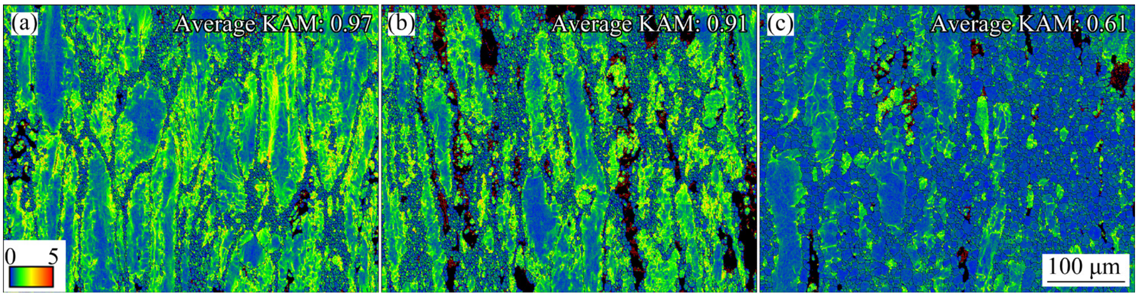

Fig. 5 KAM diagrams of alloys at different extrusion temperatures: (a) 420 °C; (b) 450 °C; (c) 480 °C

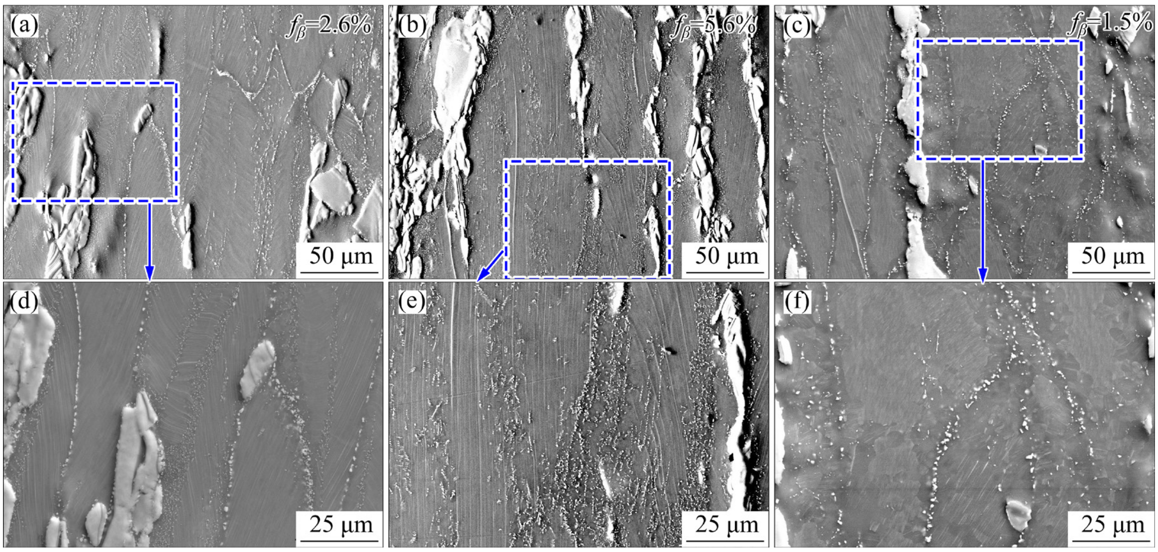

Fig. 6 SEM images of alloys at different extrusion temperatures: (a, d) 420 °C; (b, e) 450 °C; (c, f) 480 °C

process. After extrusion, the block-shaped LPSO phase is distributed along the extrusion streamline at the grain boundary, similar to the distribution of un-DRXed grains. The extrusion temperature does not significantly affect the volume fraction of the block-shaped LPSO phase. The second is the lamellar LPSO phase inside the un-DRXed grains. As mentioned, after severe plastic deformation, the LPSO phase inside the grain kinks violently and presents a streamlined distribution parallel to the extrusion direction. In addition, due to the presence of lamellar 14H-LPSO phase with narrow spacing in the primary alloy grains, the narrow-spacing characteristics of the LPSO phase are maintained in the un-DRXed grains after extrusion, potentially contributing to the subsequent strengthening effect [3]. In addition, the third type observed in the sample is the particle phase precipitated at the grain boundary during the deformation process. The volume fractions of these particle phases in the extruded alloys at 420, 450, and 480 °C are found to be 2.6%, 5.6%, and 1.5%, respectively.

The location of the dynamically precipitated phases varies depending on extrusion temperature. Figure 7 shows high-magnification SEM images of the extruded alloy at 420 °C. At this temperature, the dynamically precipitated phases are primarily located at the grain boundaries. At the un-DRX grain boundaries, these phases are about 1−2 μm in size, as indicated by the red arrows in the figure. The size of the dynamically precipitated phase generated around the DRX grains is about 0.3−0.5 μm, as indicated by the blue arrows in the figure. Previous studies by GUO et al [24] have shown that a large number of dislocations generated by deformation provide pathways for the phase precipitation, resulting in a large amount of dynamic precipitation during extrusion. In the alloy, there are more dislocations near the grain boundaries of un-DRXed grains, so the size of dynamic precipitation cannot be limited. Conversely, there are fewer dislocations near DRX grains, resulting in smaller dynamic precipitation sizes in those areas.

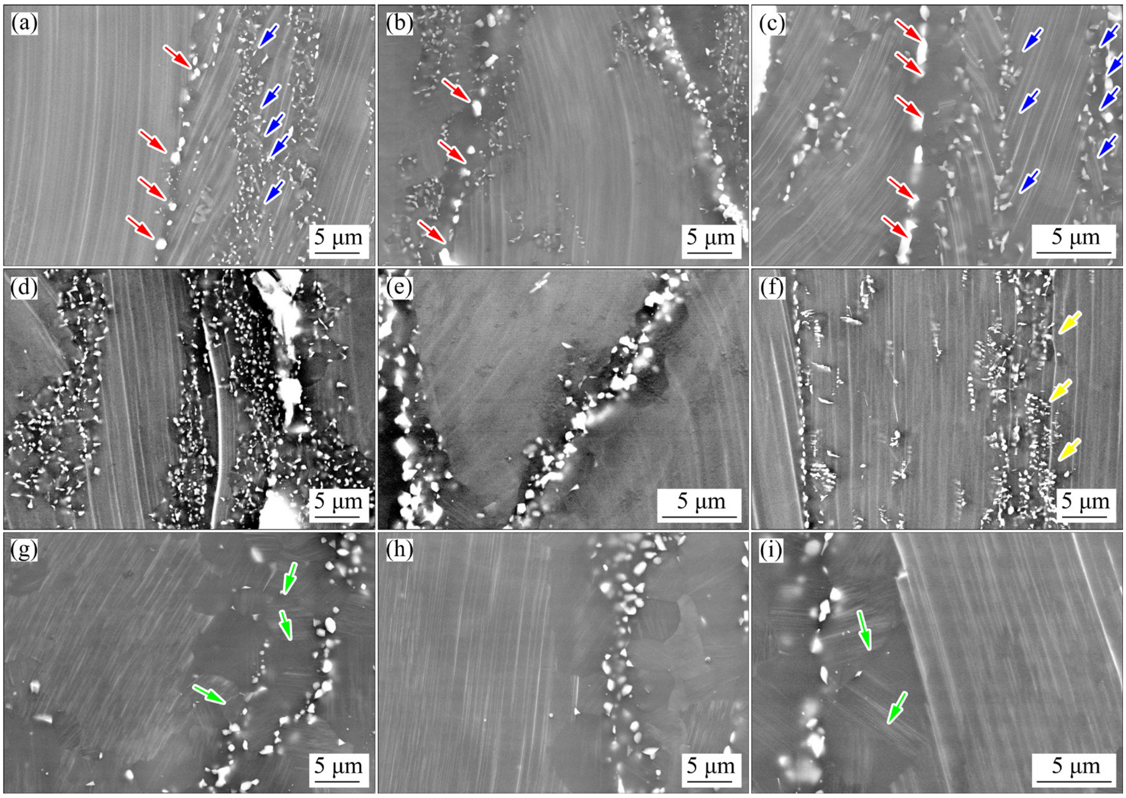

Fig. 7 Enlarged SEM images of alloys at different extrusion temperatures: (a−c) 420 °C; (d−f) 450 °C; (g−i) 480 °C

When the extrusion temperature is 450 °C, the location of dynamic precipitation changes. In addition to a large number of dynamic precipitation at the grain boundaries, there is also trace dynamic precipitation near the lamellar LPSO phase inside the un-DRXed grains, as indicated by the yellow arrows in Fig. 7. When the extrusion temperature is increased to 480 °C, the dynamic precipitation is different. In addition to a small amount of dynamically precipitated particle phase near the grain boundaries, the lamellar phase is precipitated inside the DRX grains, as indicated by the green arrows in Fig. 7.

Figure 8 further reveals that the main structure of these particle phases is the β (Mg_5RE) phase, while the lamellar phase precipitated within the DRX grains in the alloy extruded at 480 °C is the 14H-LPSO phase.

3.3 Mechanical properties

Figure 9 shows the tensile stress−strain curve of the alloys extruded at different temperatures. Table 2 summarizes the corresponding mechanical properties. For the alloy extruded at 420 °C, the tensile yield strength (TYS) is 341 MPa, the ultimate tensile strength (UTS) is 419 MPa, and the elongation (EL) is 7.2%. At an extrusion temperature of 450 °C, the tensile yield strength (TYS) is 336 MPa, the ultimate tensile strength (UTS) is 402 MPa, and the elongation (EL) is 5.6%. Finally, for the alloy extruded at 480 °C, the tensile yield strength (TYS) is 313 MPa, the ultimate tensile strength (UTS) is 388 MPa, and the elongation (EL) is 8.2%.

4 Discussion

4.1 Microstructure evolution

Figure 10 shows the feature region intercepted in Fig. 4. At a low extrusion temperature of 420 °C, most of the recrystallization sites in the extruded alloy are at the grain boundaries of parent grains, forming a necklace-like pattern around these boundaries. When the extrusion temperature rises to 450 °C, a large amount of recrystallization occurs inside the parent grains, and the grains with large deformation are thoroughly segmented by recrystallization, as indicated by the arrow in Fig. 10(c). When the extrusion temperature is 480 °C, the grain size is more uniformly distributed compared to alloys extruded at the other two temperatures.

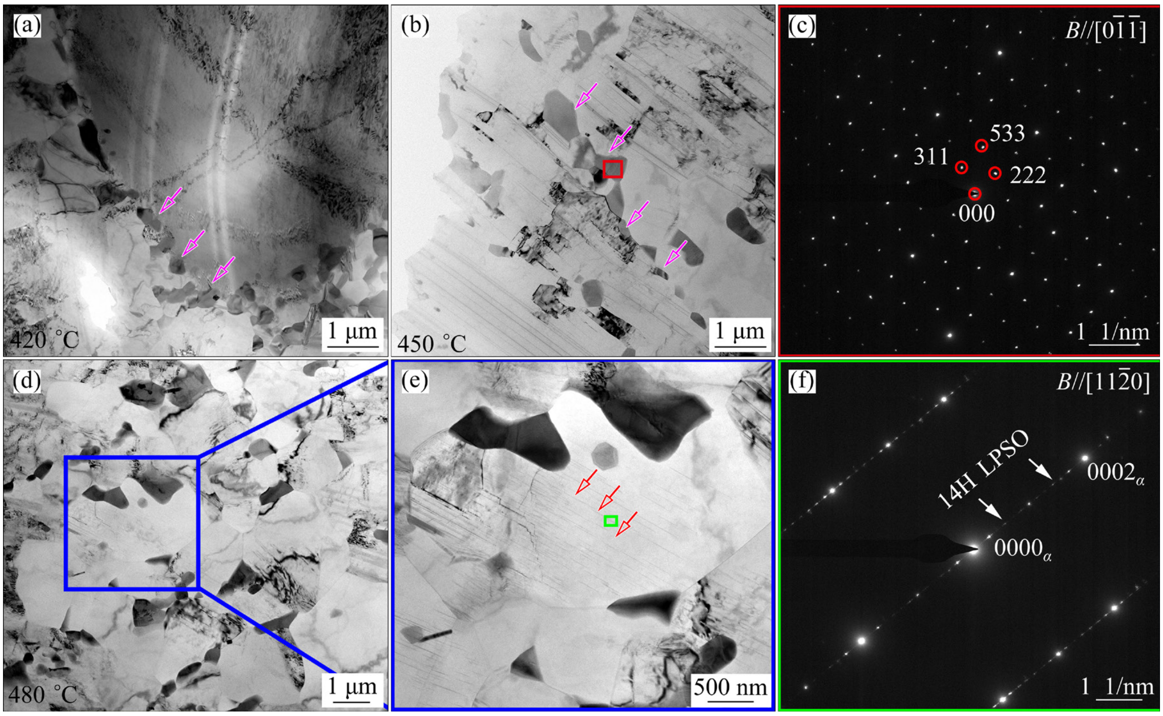

Fig. 8 TEM images of alloy extruded at 420 °C (a) and 450 °C (b), and diffraction spots of β phase (c); TEM images of alloy extruded at 480 °C (d, e) and diffraction spots of LPSO phase (f)

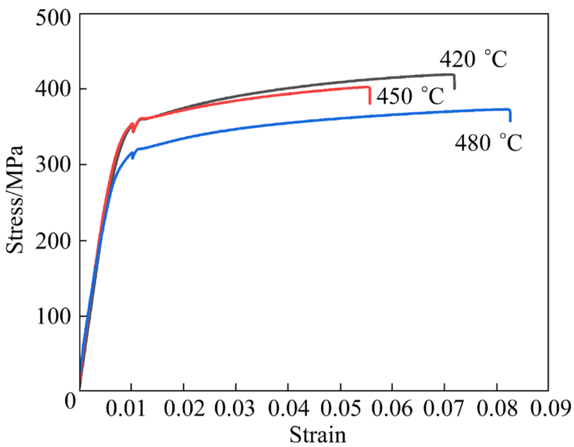

Fig. 9 Tensile stress−strain curves of alloys extruded at different temperatures

Table 2 Mechanical properties of alloys extruded at different temperatures

Extrusion temperature/°C	TYS/MPa	UTS/MPa	EL/%
420	341±2.4	419±2.2	7.2±0.2
450	336±3.2	402±2.1	5.6±0.3
480	294±2.5	373±1.8	8.2±0.5

During the extrusion, the dominant mechanism of DRX changes with the extrusion temperature. The DRX mechanism of magnesium alloys is generally divided into the continuous dynamic recrystallization (CDRX) and the discontinuous dynamic recrystallization (DDRX) [25,26]. At lower temperatures, non-uniform deformation leads to the accumulation of dislocations near the initial grain boundaries of the billet. Dislocations undergo cross-slip and climb to mitigate the increase of dislocation density, resulting in CDRX [26]. The occurrence of CDRX requires both basal slip and non-basal slip. Due to the high critical resolved shear stress (CRSS) of non-basal slip, non-basal slip tends to occur near the initial grain boundaries where the dislocation accumulation is significant. In addition, edge and screw dislocations located on the non-basal plane have higher stacking fault energy than those on the basal plane, which can be rearranged more easily and form low-angle grain boundaries (i.e., subgrains) [27,28]. The recrystallization behavior of alloys containing the LPSO phase during deformation was studied. Research indicates that the LPSO phase inhibits DDRX [29], and the narrow lamellar LPSO phase especially inhibits CDRX [30] to a certain extent. Consequently, CDRX is the predominant DRX mechanism observed in this study.

The mechanism of CDRX is closely related to dislocation activity. The *c*/*a* ratio of magnesium is 1.624, which is close to the ideal *c*/*a* ratio of a hexagonal close-packed structure (1.633). The CRSS of non-basal slip in magnesium alloy is significantly higher than that of basal slip [31]. Therefore, in low-temperature plastic deformation, the basal slip is preferentially activated through two independent slip systems, which cannot meet the five independent slip systems required for the deformation of any polycrystalline metal. By observing the dislocation density in the un-DRX region using TEM (Fig. 11(a)), we find that the sample extruded at 420 °C has a low dislocation density, with the LPSO phase hindering dislocation movement. The volume fraction of recrystallization is extremely limited under the low-temperature extrusion at 420 °C. When the temperature increases, a large number of non-basal slips are initiated, and a significant increase in dislocation density is observed in the un-DRX region of the sample extruded at 450 °C. The dislocation density in the grains increases, and the dislocations are further clustered. Following dynamic recovery at high temperatures, extensive DRX occurs within the parent grains. Further observation of the un-DRX region of the sample extruded at 480 °C reveals that most of the lamellar LPSO phase has dissolved. At this time, the obstruction of dislocation is reduced during the movement [30], allowing dislocations to move over longer distance, which facilitates the conditions necessary for recrystallization. Under high-temperature condition, DRX grains merge and grow, resulting in larger DRX grain sizes.

There have been many reports on the precipitation of β phase. The dynamic precipitation is often attributed to the nucleation of metastable phases by rare earth elements. The metastable phases act as the barriers of the newly generated

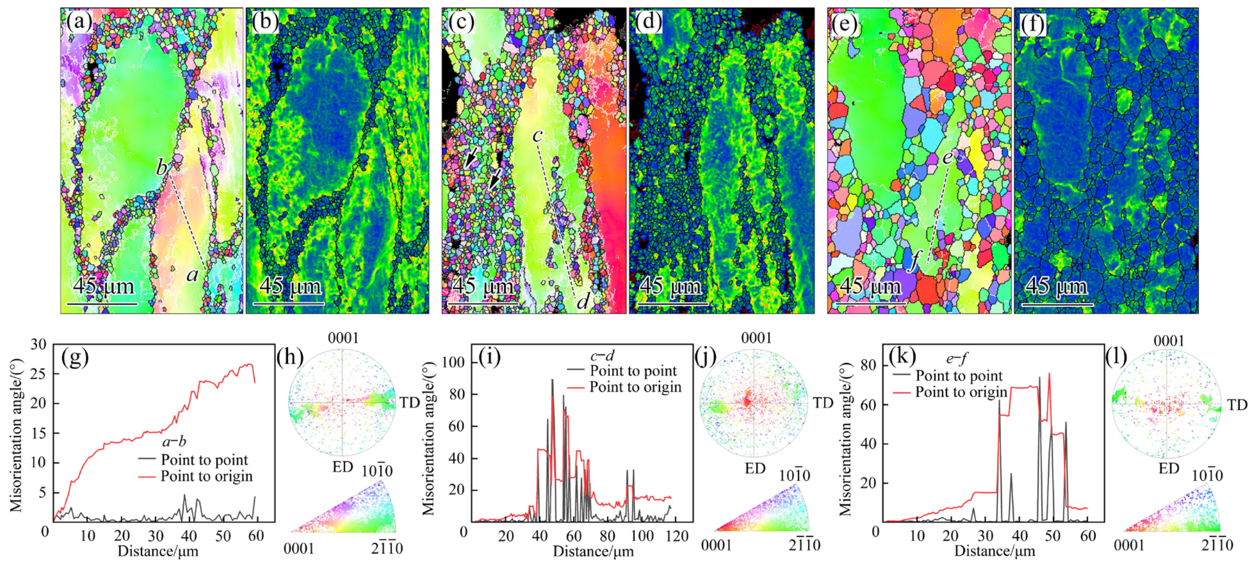

Fig. 10 IPF, KAM and PF maps, and corresponding misorientation angle diagram of alloys extruded at different temperatures: (a, b, g, h) 420 °C; (c, d, i, j) 450 °C; (e, f, k, l) 480 °C

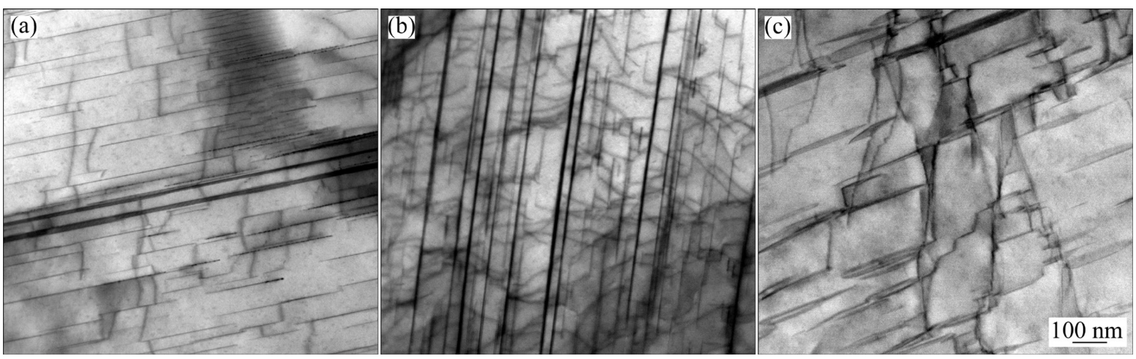

Fig. 11 Dislocation structure of alloys extruded at different temperatures: (a) 420 °C; (b) 450 °C; (c) 480 °C

dislocations, resulting in the concentration of deformation strain. It can be considered that the accumulation of deformation strain provides the driving force for the growth of metastable particles [24]. YU et al [32] found that high-density lattice defects, such as dislocations and grain boundaries, can lead to dynamic precipitation of magnesium-based alloys at high temperature. ZHANG et al [33] mentioned that dynamic precipitation occurs before DRX and limits DRX growth. When the extrusion temperature is 480 °C, due to the relationship between the growth rate and the dissolution rate, the number of β phases decreases, reducing the constraints of DRX growth. As a result, the recrystallized grain size of the alloy extruded at 480 °C is also larger. Furthermore, the type of dynamic precipitation shifts from β phase precipitation at the grain boundaries to LPSO phase precipitation within the DRX grains. LIU et al [34] studied the formation mechanism of the newly precipitated LPSO phase in dynamic recrystallization. During the hot extrusion process of Mg−RE alloy, the lamellar 14H phase gradually dissolves. The RE solute atoms first dissolve and diffuse into the α-Mg matrix, and then precipitate in the fine DRX grains due to increased stacking fault (SF). The mechanism of recrystallization and dynamic precipitation is shown in Fig. 12.

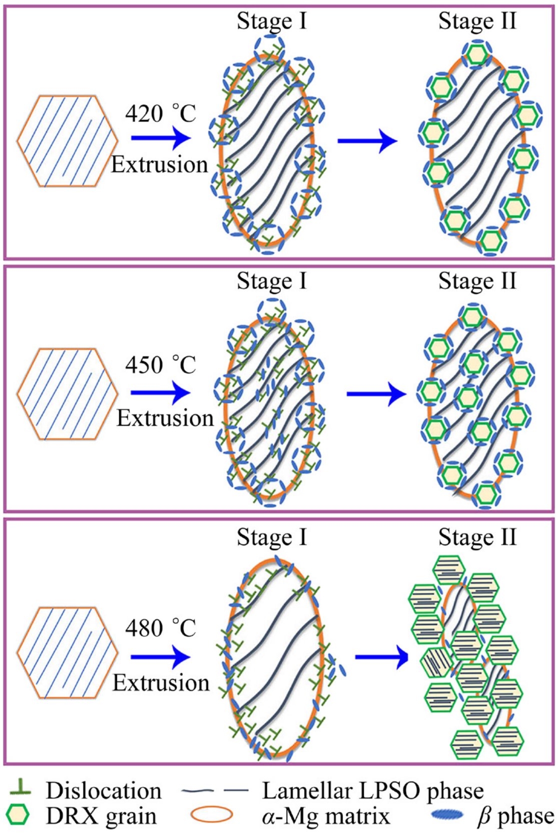

Fig. 12 Dynamic recrystallization and dynamic precipitation mechanism

4.2 Strength

Alloy strengthening includes five mechanisms: solid solution strengthening, precipitation strengthening, texture strengthening, dislocation strengthening, and grain boundary strengthening. In this study, the strengthening mechanism of extruded alloys at different temperatures is analyzed from these five aspects.

The contribution of the solid solution strengthening to the yield strength of the alloy varies depending on the amount of dynamic precipitation occurring at different temperatures. The solid solution strengthening effect can be quantified using the following formula [35]:

$$\sigma_{ss}=(\sum_i k_i^{1/n} C_i)^n \tag{1}$$

where k_i is the strengthening parameter constant of the solid solution (k_{Gd}=683 MPa and k_Y=737 MPa); C_i is the concentration of solute atoms obtained by energy spectrum analysis of the Mg matrix. The contributions of solid solution to the yield strength of the alloy extruded at 420, 450, and 480 °C are calculated to be 57, 55, and 56 MPa, respectively.

There are differences in the unDRX volume fraction of the extruded alloys at different temperatures, resulting in different volume fractions of the lamellar LPSO phase. The following formula (Eq. (2)) can be used to estimate the relative strength contribution of LPSO [3]:

$$\Delta\tau_{basal}=\frac{Gb}{2\pi\sqrt{1-v}(0.953/f_p^{1/2}-1)d_t}\ln\left(\frac{d_t}{b}\right) \tag{2}$$

where G is the shear modulus of the α-Mg matrix (about 16.6 GPa), b is the magnitude of Burgers vector (0.32 nm for Mg), v is the Poisson's ratio (v=0.32), f_p is the volume fraction of the precipitated phase, and d_t is the uniform diameter of the precipitated phase. The contributions of LPSO to the yield strength of the extruded alloy at 420, 450, and 480 °C are 30, 29, and 28 MPa, respectively.

The contribution of the relative yield strength of the block-shaped LPSO can be calculated using Eq. (3) [36]:

$$\sigma_{\mathrm{lpso}}=\Delta\sigma_{\mathrm{load}}=\frac{sV_{\mathrm{p}}}{2}\sigma_{\mathrm{m}} \tag{3}$$

where σ_m is the strength of α-Mg matrix, V_p is the volume fraction of LPSO phases (9.6% for the bulk LPSO phases, and the extrusion at different temperatures cannot change the volume fraction of the block-shaped LPSO phase), and s is the average aspect ratio of the length to diameter of block-shaped LPSO phases (measured s=3). The contributions of block-shaped LPSO to the yield strength of the extruded alloy at 420, 450, and 480 °C are 43, 43, and 37 MPa, respectively.

As mentioned above, the KAM values of extruded alloys at different temperatures are different. The following formula (Eq. (4)) can be used to estimate the contribution of dislocation density to yield strength [36]:

$$\sigma_{\mathrm{dislo}}=M\alpha Gb\sqrt{\rho} \tag{4}$$

where α is commonly 0.2 in Mg, and M is the Taylor factor of the deformed region (3.5 for Mg with strong texture). ρ is the dislocation density, which can be calculated using the following formula [36]:

$$\rho=\frac{2\Theta}{ub} \tag{5}$$

where u is the scanning step. Θ can be evaluated from the local misorientation.

The contributions of dislocations to the yield strength of alloys extruded at 420, 450, and 480 °C are 45, 43, and 35 MPa, respectively.

The grain boundary strengthening can be calculated using Hall−Petch formula [37]:

$$\sigma_{\mathrm{GB}}=kd^{-1/2} \tag{6}$$

where K is a constant of about 164 MPa, and d is the average size of recrystallized grains. It is roughly estimated that the contributions of grain boundary strengthening to yield strength of extruded alloys at 420, 450, and 480 °C are 34, 35, and 37 MPa, respectively.

Due to the extrusion ratio of 3.6:1 in this experiment, there is a strong extrusion texture in the extruded alloy, and the texture strengthening occupies a large contribution. However, the texture intensity of the extruded alloys at three temperatures is different, and the texture-strengthening effect can be estimated using the following formula:

$$\sigma_{\mathrm{T}}=\sigma_{\mathrm{y}}-\sigma_{\mathrm{ss}}-\sigma_{\mathrm{LPSO}}-\sigma_{\mathrm{dislo}}-\sigma_{\mathrm{GB}} \tag{7}$$

The contributions of texture to the yield strength of the alloy extruded at 420, 450, and 480 °C are 132, 130, and 101 MPa, respectively.

Based on the calculations above, the improvement in the strength of extruded magnesium alloys at different temperatures can be primarily attributed to two factors. First, all extruded alloys exhibit a bimodal structure composed of fine DRX grains and coarse un-DRX grains. There is a strong basal texture in un-DRX. It has been reported that magnesium alloys with strong basal texture can be significantly strengthened by hindering the activation of substrate slip when loaded along ED [38,39]. Therefore, the strong basal texture obtained in all as-extruded alloys contributes to their high TYS. Secondly, in the extruded alloy, the dislocation density in the un-DRX region is significantly higher than that in the DRX region. Un-DRX grains with high dislocation density enhance TYS during tensile deformation through a strain-hardening effect [40].

The microstructure obtained by extrusion at 420 °C has the strongest texture and significant dislocations within the un-DRXed grains. The degree of dynamic recrystallization increases as extrusion temperature increases (450 °C). However, in the system dominated by texture strengthening and dislocation strengthening, the DRX fraction is increased to improve the grain boundary strengthening of DRX grains while reducing the strengthening effect of un-DRX grains. In this case, the increase of grain boundary strengthening cannot make up for the decrease of the un-DRX

Table 3 Strengthening contributions

Extrusion temperature/°C	Solid solution strengthening/MPa	LPSO strengthening/MPa	Texture strengthening/MPa	Dislocation strengthening/MPa	Grain boundary strengthening/MPa
420	57	73	132	45	34
450	55	72	130	44	35
480	51	65	101	40	37

strengthening effect, leading to a decrease in yield strength. Although the recrystallization fraction further improves at an extrusion temperature of 480 °C, the large-sized recrystallized grains weaken the effects of grain boundary strengthening, texture strengthening, and dislocation strengthening.

4.3 Ductility

Figure 13 shows the SEM images near the fracture position. It can be observed that the microcracks appear near the β phase. These brittle eutectic phases, acting as crack-forming phases (CFPs), restrict the rotation of grains during tensile deformation, leading to stress concentration and premature fracture [41]. YU et al [38] reported that the higher volume fraction of Mg_5RE particles in the alloy can reduce the ductility of the alloy. This phenomenon is also found in this study. The micro-cracks are observed near the β phase at the grain boundaries in the alloy extruded at 420 °C, whereas in the alloy extruded at 450 °C, micro-cracks are found both at the grain boundary and at the intragranular β phase, which is consistent with the β phase precipitation position discussed above. In addition, according to statistics, the volume fraction of β phase of the alloy extruded at 420 °C is 2.6%, and its elongation is 7.2%, while the volume fraction of β phase of the alloy extruded at 450 °C is 5.6%, and its elongation is 5.6%. It is also shown that the volume fraction of the β phase significantly affects the elongation of the extruded alloy.

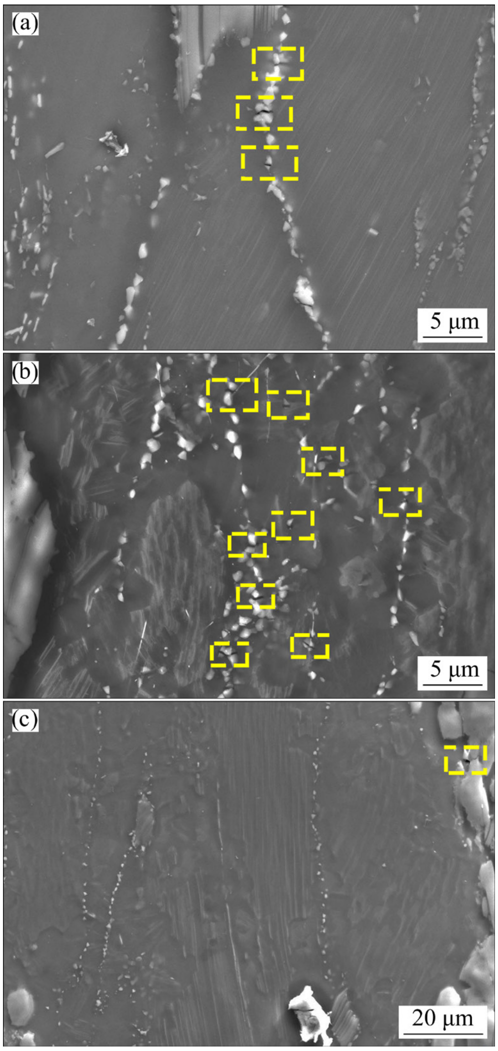

Fig. 13 SEM images of crack initiation near fracture position in alloys extruded at different temperatures: (a) 420 °C; (b) 450 °C; (c) 480 °C

Moreover, in the alloy extruded at 480 °C, few microcracks are observed, and the elongation reaches 8.2%. This increased elongation can be attributed to two factors. On the one hand, the number of β dynamic precipitation phases in the extruded alloy at 480 °C is minimal and uniformly dispersed, which can alleviate the local stress concentration around the particles. Additionally, the increase in DRX fraction can also reduce the initiation of microcracks and delay the propagation of cracks [34]. This observation is consistent with findings by YANG et al [14], who reported that the decrease in the volume fraction of fine particles and the increase of DRX fraction in high-temperature extruded alloys can reduce the initiation of microcracks and delay the propagation of cracks. On the other hand, a large number of dynamic precipitates of the LPSO phase are found within the DRX grains of the alloy extruded at 480 °C.

5 Conclusions

(1) The volume fraction of DRX increases with increasing extrusion temperature. With the increase of DRX volume fraction, the texture strength diminishes, and the density of dislocations within the grains decreases.

(2) At an extrusion temperature of 420 °C, the β phase only precipitates along the DRX grain boundaries. At an extrusion temperature of 450 °C, β phase precipitates not only at DRX grain boundaries but also within the un-DRX grains. At this temperature, the volume fraction of the β phase reaches its maximum.

(3) Increase in strength is mainly caused by

strong texture and pinning of internal dislocations in the un-DRX zone. As the extrusion temperature rises, the texture weakens, and the density of dislocations in the un-DRX regions decreases, leading to a reduction in yield strength. A large number of β phase particles act as crack sources and provide pathways for crack extension at grain boundaries. The optimum mechanical properties of the alloy are obtained with extrusion at 420 °C, yielding a tensile yield strength of 341 MPa, an ultimate tensile strength of 419 MPa, and a fracture elongation of 7.2%.

CRediT authorship contribution statement

Ya-yun HE: Conceptualization, Data curation, Formal analysis, Writing − Original draft; **Rui GUO:** Conceptualization, Methodology, Resources, Writing − Review & editing, Funding acquisition; **Xi ZHAO:** Conceptualization, Methodology, Writing − Review & editing; **Zhi-min ZHANG:** Writing − Review & editing.

Declaration of competing interest

The authors declare that they have no known competing financial interests or personal relationships that could have appeared to influence the work reported in this paper.

Acknowledgments

The authors gratefully acknowledge the financial support by the Innovative Talents Support Program of Higher Education Institutions in Shanxi Province, China, and Project of Science and Technology by the North University of China in 2022 (No. 20221878).

References

[1] XU Jian, ZHENG Jie, LIU Wan-er, HUANG You-wang, YAN Zhao-ming, ZHANG Zhi-min, WANG Qiang, XUE Yong. Recrystallization behavior and strengthening mechanism of extruded Mg−Gd−Y−Zn−Zr alloy with different pre-aged states [J]. Transactions of Nonferrous Metals Society of China, 2024, 34(2): 480−503.

[2] YOSHIHITO K, KENTARO H, AKIHISA I, TSUYOSHI M. Rapidly solidified powder metallurgy $Mg_{97}Zn_1Y_2$ alloys with excellent tensile yield strength above 600 MPa [J]. Materials Transactions, 2001, 42(7): 1172−1176.

[3] XU Chao, NAKATA T, QIAO Xiao-guang, ZHENG Ming-yi, WU Kun, KAMADO S. Effect of LPSO and SFs on microstructure evolution and mechanical properties of Mg−Gd−Y−Zn−Zr alloy [J]. Scientific Reports, 2017, 7(1): 1−10.

[4] HAGIHARA K, SUGINO Y, FUKUSUMI Y, UMAKOSHI Y, NAKANO T. Plastic deformation behavior of $Mg_{12}ZnY$ LPSO-phase with 14H-typed structure [J]. Materials Transactions, 2011, 52(6): 1096−1103.

[5] WU Jing, IKEDA K C, SHI Q, CHIU Yu-lung. Kink boundaries and their role in dynamic recrystallisation of a Mg−Zn−Y alloy [J]. Materials Characterization, 2019, 148: 233−242.

[6] CHEN Xin, LI Si-long, WAN Ying-chun. Effect of Gd on preparation of nanocrystalline Mg alloys via cold rotary swaging [J]. Transactions of Nonferrous Metals Society of China, 2024, 34(6): 1817−1828.

[7] WU Xiao-feng, XU Chun-xiang, ZHANG Zheng-wei, YANG Wen-fu, ZHANG Jing-shan. Microstructure evolution, strengthening mechanisms and deformation behavior of high-ductility Mg−3Zn−1Y−1Mn alloy at different extrusion temperatures [J]. Transactions of Nonferrous Metals Society of China, 2023, 33(2): 422−437.

[8] RAMALINGAM V V, RAMASAMY P, KOVUKKAL M D, MYILSAMY G. Research and development in magnesium alloys for industrial and biomedical applications: A review [J]. Metals Materials International, 2020, 26: 409−430.

[9] SUN Wan-ting, HE Yang, QIAO Xiao-guang, ZHAO Xiao-jun, CHEN Hou-wen, GAO Nong, STARINK M J, ZHENG Ming-yi. Exceptional thermal stability and enhanced hardness in a nanostructured Mg−Gd−Y−Zn−Zr alloy processed by high pressure torsion [J]. Journal of Magnesium Alloys, 2023, 11(12): 4589−4602.

[10] XU C, NAKATA T, FAN G H, Li X W, TANG G Z, GENG L, KAMADO S. Microstructure and mechanical properties of extruded Mg−Gd−Y−Zn alloy with Mn or Zr addition [J]. Journal of Materials Science, 2019, 54: 10473−10488.

[11] XU Wen-long, SU Chang, CHEN Xian-hua, HAN Xiu-zhu, ZHANG Gao-long, Pan Fu-sheng. Tailoring precipitates in Mg−12Gd−3Y alloys by Sn addition to obtain superior elevated temperature mechanical properties [J]. Materials Science Engineering A 2023, 873: 145006.

[12] YU Zi-jian, XU Chao, MENG Jian, LIU Ke, FU Jin-long, KAMADO S. Effects of extrusion ratio and temperature on the mechanical properties and microstructure of as-extruded Mg−Gd−Y−(Nd/Zn)−Zr alloys [J]. Materials Science and Engineering A, 2019, 762: 138080.

[13] ZHENG Jie, CHEN Zhe, YAN Zhao-ming, ZHANG Zhi-min, WANG Qiang, XUE Yong. Preparation of ultra-high strength Mg−Gd−Y−Zn−Zr alloy by pre-ageing treatment prior to extrusion [J]. Journal of Alloys Compounds, 2022, 894: 162490.

[14] YANG Zhao, XU Chao, NAKATA T, SHIGEHARU K. Effect of extrusion ratio and temperature on microstructures and tensile properties of extruded Mg−Gd−Y−Mn−Sc alloy [J]. Materials Science and Engineering A, 2021, 800: 140330.

[15] ZHAI Hao-wei, LI Wang, WANG Qing-hang, LI Meng, CHAI Yan-fu, XU Jun, JIANG Bin. Achieving high strength near 400 MPa in an ultra-fine grained Mg–Bi–Ca ternary alloy via low-temperature extrusion [J]. Journal of Materials Research and Technology, 2023, 26: 3973−3991.

[16] SADEGHI A, PEKGULERYUZ M. Effect of pre-deformation anneal on the microstructure and texture evolution of Mg−3Al−1Zn−0.7 Sr alloy during hot extrusion [J]. Journal of Materials Science, 2012, 47: 5374−5384.

[17] CHEN Yong-jun, WANG Qu-dong, PENG Jiang-guo, ZHAI Chun-quan, DING Wen-jaing. Effects of extrusion ratio on the microstructure and mechanical properties of AZ31 Mg alloy [J]. Journal of Materials Processing Technology, 2007, 182(1/2/3): 281−285.
[18] SHAHZAD M, WAGNER L. Influence of extrusion parameters on microstructure and texture developments, and their effects on mechanical properties of the magnesium alloy AZ80 [J]. Materials Science Engineering A, 2009, 506: 141−147.
[19] HUANG, Xin-sheng, CHINO Y, YUASA M, UEDA H, INOUE M, KIDO F, MATSUMOTO T. Microstructure and mechanical properties of AZX912 magnesium alloy extruded at different temperatures [J]. Materials Science Engineering A, 2017, 679: 162−171.
[20] SUN Yue-hua, ZHANG Fan, YANG Bin, REN Jian, SONG Guang-sheng. Effect of extrusion ratio on microstructure, texture, and mechanical properties of dual-phase Mg−8Li−6Zn−2Gd alloy [J]. Transactions of Nonferrous Metals Society of China, 2024, 34(3): 833−845.
[21] CHEN Han, HU Zhang, HAN Yu-xiang, CHEN Tao, LIU Chu-ming, CHEN Zhi-yong. Microstructure and mechanical properties of Mg−Gd−Y−Zn−Zr alloy plates with different initial textures after hot rolling [J]. Transactions of Nonferrous Metals Society of China, 2024, 34(6): 1804−1816.
[22] LI R G, LI H R, PAN H C, XIE D S, ZHANG J H, FANG D Q, DAI Y Q, ZHAO D Y, ZHANG H. Achieving exceptionally high strength in binary Mg−13Gd alloy by strong texture and substantial precipitates [J]. Scripta Materialia, 2021, 193: 142−146.
[23] HAO Jian-qiang, ZHANG Jin-shan, LI Bo-qiong, XIE Rui-zhen. Effects of 14H-LPSO phase on the dynamic recrystallization and work hardening behaviors of an extruded Mg–Zn–Y–Mn alloy [J]. Materials Science and Engineering A, 2021, 804: 140727.
[24] GUO Fei, ZHANG Ding-fei, YANG Xu-sheng, JIANG Lu-yao, PAN Fu-sheng. Strain-induced dynamic precipitation of $Mg_{17}Al_{12}$ phases in Mg−8Al alloys sheets rolled at 748 K [J]. Materials Science and Engineering A, 2015, 636: 516−521.
[25] GALIYEV A, KAIBYSHEV R, GOTTSTEIN G. Correlation of plastic deformation and dynamic recrystallization in magnesium alloy ZK60 [J]. Acta Materialia, 2001, 49: 1199−1207. (in German)
[26] SITDIKOV O, KAIBYSHEV R. Dynamic recrystallization in pure magnesium [J]. Materials Transactions, 2001, 42(9): 1928−1937.
[27] SMITH A. Surface, interface and stacking fault energies of magnesium from first principles calculations [J]. Surface Science, 2007, 601(24): 5762−5765.
[28] BISWAS S, DHINWAL S, SUWAS S. Room-temperature equal channel angular extrusion of pure magnesium [J]. Acta Materialia, 2010, 58: 3247−3261.
[29] ZHOU Xiao-jie, LIU Chu-ming, GAO Yong-hao, JIANG Shu-nong, Xiu-zhu Han, CHEN Zhi-yong. Evolution of LPSO phases and their effect on dynamic recrystallization in a Mg−Gd−Y−Zn−Zr alloy [J]. Metallurgical and Materials Transactions A, 2017, 48: 3060−3072.
[30] LI Ji-yu, WANG Fu-lin, ZENG Jian, ZHAO Chao-yu, JIN Li, DONG Jie. Effect of the interspacing of intragranular lamellar LPSO phase on dynamic recrystallization behaviors of Mg−Gd−Y−Zn−Zr alloys [J]. Materials Characterization, 2022, 193: 112326.
[31] KOIKE J, KOBAYASHI T, MUKAI T, WATANABE H, SUZUKI M, MARUYAMAK, HIGASHI K. The activity of non-basal slip systems and dynamic recovery at room temperature in fine-grained AZ31B magnesium alloys [J]. Acta Materialia, 2003, 51: 2055−2065.
[32] YU Zi-jian, XU Chao, MENG Jian, KAMADO S. Micro-structure evolution and mechanical properties of a high strength Mg−11.7Gd−4.9Y−0.3Zr (wt.%) alloy prepared by pre-deformation annealing, hot extrusion and ageing [J]. Materials Science and Engineering A, 2017, 703: 348−358.
[33] ZHANG Qian, LI Quan-an, Chen Xiao-ya, ZHAO Jia-xin, BAO Jian, CHEN Zi-yi. Dynamic precipitation and recrystallization mechanism during hot compression of Mg−Gd−Y−Zr alloy [J]. Journal of Materials Research and Technology, 2021, 15: 37−51.
[34] LIU Wei, ZHAO Yu-hong, ZHANG Yun-tao, SHUAI Chuan, CHEN Li-wen, HUANG Zhi-quan, HOU Hua. Deformation-induced dynamic precipitation of 14H-LPSO structure and its effect on dynamic recrystallization in hot-extruded Mg−Y−Zn alloys [J]. International Journal of Plasticity, 2023, 164: 103573.
[35] ZHA Min, MA Xiao, JIA Hai-long, HUA Zhen-ming, FAN Zhao-xu, YANG Zhi-zheng, GAO Yi-peng, WANG Hui-yuan. Dynamic precipitation and deformation behaviors of a bimodal-grained WE43 alloy with enhanced mechanical properties [J]. International Journal of Plasticity, 2023, 167: 103682.
[36] KWAK T, KIM W. Mechanical properties and Hall−Petch relationship of the extruded Mg−Zn−Y alloys with different volume fractions of icosahedral phase [J]. Journal of Alloys and Compounds, 2019, 770: 589−599.
[37] ZHENG Jie, CHEN Zhe, YAN Zhao-ming, ZHANG Zhi-min, XUE Yong. An alternating ageing-annealing process for enhancing strength and ductility of a Mg−Gd−Y−Zn−Zr alloy [J]. Materials Science and Engineering A, 2021, 828: 142103.
[38] YU Zi-jian, XU Chao, MENG Jian, ZHANG Xu-hu, KAMADO S. Microstructure evolution and mechanical properties of as-extruded Mg−Gd−Y−Zr alloy with Zn and Nd additions [J]. Materials Science and Engineering A, 2018, 713: 234−243.
[39] BARNETT M. Twinning and the ductility of magnesium alloys: Part I: “Tension” twins [J]. Materials Science and Engineering A, 2007, 464: 1−7.
[40] SEDLÁČEK R, BLUM W, KRATOCHVIL J, FOREST S. Subgrain formation during deformation: Physical origin and consequences [J]. Metallurgical and Materials Transactions A, 2002, 33: 319−327. (in German)
[41] SONG Ming, HE Yue-hui, WU Zheng-gang, HUANG Bai-yun. Multi-scale model for the ductility of multiple phase materials [J]. Mechanics of Materials, 2009, 41(5): 622−633.

通过低温和小挤压比变形制备高强韧 Mg−Gd−Y−Zn−Zr 合金

贺亚云[1]，郭 睿[2]，赵 熹[1,2]，张治民[3]

1. 中北大学 机电工程学院，太原 030051；
2. 中北大学 航空宇航学院，太原 030051；
3. 中北大学 材料科学与工程学院，太原 030051

摘 要：采用预先调控片层长程有序(LPSO)相的方法来增强稀土镁合金的热加工能力。此外，采用低温挤压实现小变形程度下合金性能的综合提升，为高性能大型构件的制备提供新的途径。对比分析了不同温度 (420、450、480 ℃) 挤压 (挤压比为 3.6:1) 对 Mg−Gd−Y−Zn−Zr 合金显微组织和性能的影响，以阐明低温挤压下的强化和塑性机制。结果表明，挤压温度为 420 ℃时，合金的屈服强度为 341 MPa，抗拉强度为 419 MPa，伸长率为 7.2%。强度的提高主要得益于未动态再结晶区(un-DRX)较强的基面织构和内部位错钉扎，较低的 β 动态析出相体积分数有利于提高合金的塑性。

关键词：14H-LPSO 层片相；Mg−Gd−Y−Zn−Zr 合金；低温挤压；β 动态析出相

(Edited by Bing YANG)